

Numerical Simulation of Viscous-like Flow in and Around the Plasma Tail of a Comet

M. Reyes-Ruiz¹, H. Pérez-de-Tejada², H. Aceves¹, and R. Vázquez¹

¹ Instituto de Astronomía, Universidad Nacional Autónoma de México, Apdo Postal 877,
Ensenada 22800, B.C., México

e-mail: maurey, aceves, vazquez@astro.unam.mx,

² Instituto de Geofísica, Universidad Nacional Autónoma de México, Ciudad Universitaria, C.P.
04510, México D.F.

e-mail: perezdet@geofisica.unam.mx

Received September 15, 1996; accepted March 16, 1997

ABSTRACT

Aims. To model the interaction of the solar wind with the plasma tail of a comet by means of numerical simulations, taking into account the effects of viscous-like forces.

Methods. A 2D hydrodynamical, two species, finite difference code has been developed for the solution of the time dependent continuity, momentum and energy conservation equations, as applied to the problem at hand.

Results. We compute the evolution of the plasma of cometary origin in the tail as well as the properties of the shocked solar wind plasma around it, as it transfers momentum on its passage by the tail. Velocity, density and temperature profiles across the tail are obtained. Several models with different flow parameters are considered in order to study the relative importance of viscous-like effects and the coupling between species on the flow dynamics. Assuming a Mach number equal to 2 for the incident solar wind as it flows past the comet's nucleus, the flow exhibits three transitions with location and properties depending on the Reynolds number for each species and on the ratio of the timescale for inter-species coupling to the crossing time of the free flowing solar wind. By comparing our results with the measurements taken *in situ* by the Giotto spacecraft during its flyby of comet Halley we constrain the flow parameters for both plasmas.

Conclusions. In the context of our approximations, we find that our model is qualitatively consistent with the *in situ* measurements as long as the Reynolds number of the solar wind protons and of cometary H₂O⁺ ions is low, less than 100, suggesting that viscous-like momentum transport processes may play an important role in the interaction of the solar wind and the plasma environment of comets

Key words. comets – solar wind — Hydrodynamics — comets: Halley – comet Giacobinni-Zinner – methods numerical

1. Introduction

The nature of the interaction of the solar wind with the plasma environment of comets as they approach the Sun, has been under investigation since the early days of space physics as a discipline (Biermann 1951, Alfvén 1957, see reviews by Cravens & Gombosi 2004, and Ip 2004). The basic elements of the interaction were developed in the 20 years following the work of Biermann (1951), who proposed that the interaction between the solar wind and the comet’s plasma is responsible for the observed aberration angle of plasma tails with respect to the Sun-comet radius vector. Based on the inefficiency of Coulomb collisional processes in the coupling of the solar wind and cometary plasmas, Alfvén (1957) proposed that the interplanetary magnetic field (IMF) is a fundamental ingredient in the solar wind-comet interaction; being responsible for channelling the cometary ions as it drapes into a magnetic tail. Biermann et al. (1967) suggested that as cometary ions are created and incorporated (picked-up) into the solar wind, the loading of the flow with this additional mass results in a modification of the flow properties as the solar wind approaches a comet; an idea further developed by Wallis (1973) (for a review see Szego et al. 2000). The IMF and mass loading are thus the main dynamical agents generally considered when developing models for the interaction of the solar wind with cometary ionospheres, as well as with other solar system bodies having an ionosphere and without a strong intrinsic magnetic field.

However, as has been pointed out by Perez-de-Tejada et al. (1980) and Perez-de-Tejada (1989), several features of the flow dynamics in the cometosheath and plasma tail of comets can be attributed to the action of viscous-like forces as the solar wind interacts with cometary plasma. Such interaction processes are believed to be similar to those known to be occurring in other solar system bodies that have an ionosphere and no significant intrinsic magnetic field, particularly Venus and Mars (for a review see Perez-de-Tejada 1995, Perez-de-Tejada 2009 and references therein). *In situ* measurements indicate that, as in Venus and Mars, the solar wind flow in the ionosheath of comet Halley exhibits an intermediate transition, also called the “mystery transition”, located approximately half-way between the bow shock and the cometopause (Johnstone et al. 1986, Goldstein et al. 1986, Reme 1991, Perez-de-Tejada 1989 and references therein). Below this transition, as we approach the cometopause, the antisunward velocity of the shocked solar wind decreases in a manner consistent with a viscous boundary layer (Perez-de-Tejada 1989). Also indicative of the presence of viscous-like processes is that the temperature of the gas increases, and the density decreases, as we move from the intermediate transition to the cometopause. Taking the distance between the intermediate transition and the cometopause as the thickness of a viscous boundary layer, which depends on the effective Reynolds number of the flow (R_{eff}), Perez-de-Tejada (1989) estimated that $R_{\text{eff}} \approx 300$ for the solar wind flow in the cometosheath is necessary to reproduce the flow properties measured *in situ* by the Giotto spacecraft on its flyby of comet Halley.

An additional argument suggesting the importance of viscous-like effects in the dynamics of the flow in the cometosheath and tail regions, follows from the comparison of the magnitude of the terms corresponding to momentum transport due to viscous-like forces and $\mathbf{J} \times \mathbf{B}$ forces in the momentum conservation equation. Perez-de-Tejada (1999, 2000) has argued that downstream from the terminator in the ionosheath of Venus, a scenario analogous to the one considered in this paper, the fact that the flow is superalfvenic, as found from the *in situ* measurements of the Mariner

5 and Venera 10 spacecraft, suggests that viscous-like forces may dominate over $\mathbf{J} \times \mathbf{B}$ forces in the flow dynamics in the boundary layer formed in the interaction of solar wind and ionospheric plasma. If the flow is characterized by a low effective Reynolds number, R_{eff} , this layer extends over a significant portion of the ionosheath of the planet.

In comets, *in situ* measurements obtained during the passage of the ICE spacecraft through the tail of comet Giacobinni-Zinner (Bame et al. 1986, Slavin et al. 1986, Meyer-Vernet 1986, Reme 1991) indicate that along the inbound trajectory (which lies slightly tailward of the comet nucleus) the magnetic field in the so-called transition and sheath regions, is approximately 10 nT, the number density is approximately 10 cm^{-3} and the tailward flow velocity varies from $\sim 400 \text{ km/s}$ (near the bow shock) down to 100 km/s . According to Perez-de-Tejada (1999), the ratio of viscous-like to magnetic forces is essentially the square of the alfvénic Mach number, $M_A^2 = V^2/(B^2/8\pi\rho)$. From the data of the ICE spacecraft cited above, we find that M_A^2 ranges between 4 and 40 across the cometsheath and hence, viscous-like stresses may dominate over $\mathbf{J} \times \mathbf{B}$ forces by a similar amount, or more, throughout the cometsheath region tailward of the nucleus. In the vicinity of the plasma tail, the measurements of the ICE spacecraft (Bame et al. 1986, Slavin et al. 1986) indicate that the midplane density, dominated by cometary ions, reaches values of 200 cm^{-3} at the point where the magnetic field is a maximum 50 nT. With flow speeds of approximately 20 km/s , the square of the alfvénic Mach number reaches a minimum value of 2-3 so that, even in the plasma tail, viscous-like forces are, at least, as important as $\mathbf{J} \times \mathbf{B}$ forces following the arguments of Perez-de-Tejada (1999).

The fact that $M_A^2 \gg 1$ in the cometsheath means that the magnetic energy density is much smaller than the kinetic energy associated with the inertia of the plasma. This implies that $\mathbf{J} \times \mathbf{B}$ forces are not the dominant dynamical factor responsible for the large scale properties of the flow in the region. In fact, one can argue that the formation of a magnetic tail is an indication that in the cometsheath, the large-scale magnetic field does not dominate the dynamics, it is merely carried around by the superalfvénic flow. If the dynamics were controlled by the magnetic forces, field lines would not bend onto a magnetic tail and the direction of the ion tail would not be essentially in the direction of the local solar wind velocity. We believe that the magnetic field does play a crucial role in the momentum transfer between the solar wind and the cometary plasma, but it is the small scale, “turbulent” magnetic field component, that mediates the microscopic interaction between charged particles leading to the transfer of momentum that we are modelling as an effectively viscous process.

1.1. On the origin of “viscosity”

The precise origin of the viscous-like momentum transfer processes invoked in the viscous flow interpretation of the intermediate transition, in the ionosheath of comet Halley and in other ionospheric obstacles to the solar wind, is not yet clear. Typical properties of solar wind and cometsheath plasma result in a “normal” viscosity, as it appears in the Navier-Stokes equations when derived from Boltzmann’s equation, that can be considered negligible in the flow dynamics. Using for example properties of the shocked solar wind in the vicinity of the tail measured at comet Giacobinni-Zinner, $n_i = 10 \text{ cm}^{-3}$, $|B| = 10 \text{ nT}$ and $T = 3 \times 10^5 \text{ K}$ (Bame et al. 1986, Slavin et al. 1986) one calculates the viscosity coefficient resulting from particle interactions according to Spitzer (1962, eqn. 5-55) to be $\mu \sim 10^{17} \text{ g cm}^{-1} \text{ s}^{-1}$. This extremely low value most likely repre-

sents a lower limit for the viscosity coefficient, since it reflects the ability to transport momentum across field lines in a plasma threaded by a strong, uniform magnetic field. A more appropriate expression for the plasma viscosity coefficient in the conditions of a cometsheath is probably given by the coefficient presented in Cravens et al. (1980), which corresponds to a plasma in a strongly fluctuating magnetic field. Perez-de-Tejada (2005) has calculated the viscosity coefficient for the ionosheath of Venus based on these results. If we use the same procedure to calculate the viscosity coefficient for the solar wind around the tail of a comet (with the conditions measured at Giacobini-Zinner) we find $\mu \sim 10^{-11} \text{ g cm}^{-1} \text{ s}^{-1}$.

With typical values for the solar wind velocity and mass density in the cometsheath around the tail of comet Giacobini-Zinner, $V = 200 \text{ km/s}$ and $\rho = 1.67 \times 10^{-23} \text{ gm cm}^{-3}$ respectively (Bame et al. 1986), and adopting a characteristic lengthscale of 10^5 km for the variation of the flow velocity (roughly the thickness of the sheath region), we find that the corresponding Reynolds number for the flow, based on the “normal” viscosity coefficient estimated above, is $Re > 10^5$. This indicates that viscous effects resulting from the collisions between particles in this environment are negligible. Assuming that the Prandtl number is not very different from unity, as argued by Perez-de-Tejada (2005), we can also neglect heat conduction resulting from particle collisions.

However, as in Venus and Mars, strong turbulence has been measured in the ionosheath of comets Halley and Giacobini-Zinner (Baker et al. 1986, Scarf et al. 1986, Klimov et al. 1986, Tsurutani and Smith 1986) and, as it generally occurs in many fluid dynamics applications, turbulence is characterized (sometimes even defined) by a dramatic increase in the efficiency of transport processes, viscosity included, in the flow (Lesieur 1990). The likely importance of turbulent viscosity in this scenario is also expected in view of the large value of the Reynolds number estimated above. Also, as discussed by Shapiro et al. (1995) and Dobe et al. (1999 and references therein) conditions in the ionosheath of Venus and Mars favour the development of plasma instabilities leading to effective wave-particle interactions. If this mechanism operates also in the cometsheath, it may lead, as in these planets, to increased coupling between the solar wind and cometary plasma in a viscous-like manner as suggested by Perez-de-Tejada (1989). In our opinion this justifies a detailed study of the hypothesis of viscous-like effects on the flow dynamics in solar wind-comet interactions. It is the purpose of this paper to begin these investigations.

In this paper we present results of 2D hydrodynamical, numerical simulations of the flow of solar wind and cometary H_2O^+ ions in the tail and tailward cometsheath of a comet. This is our first attempt to model the interaction of the solar wind with the plasma environment of a comet taking into account viscous-like forces which. We review the estimation of the effective Reynolds number of Perez-de-Tejada (1989), based on the comparison of *in situ* measurements at comet Halley with results from numerical simulations of the viscous-like, compressible flow of the solar wind over a dense, cold and slow velocity gas representing the plasma tail of a comet. We also study the relative importance of viscous-like forces and the coupling between the fast moving protons of the solar wind and the slow H_2O^+ ions in the tail. We do the latter by comparing models with different values of the effective Reynolds number, the parameter controlling viscous-like effects, and the effective coupling timescale between both species.

The paper is organized as follows. In section 2 we present the formulation of the problem, the basic equations, approximations and parameters. Section 3 presents results of a series of simulations with different model parameters. A comparison of our results with *in situ* measurements at

comet Halley is discussed in section 4. Finally, in section 5 we summarize our main results and present our conclusions.

2. Formulation of the problem

We model the interaction of the solar wind with the plasma tail of a comet using a 2D hydrodynamic, two species (a and b), finite difference code that is an extension of the single species version presented in Reyes-Ruiz et al. (2008). Included in the dynamical equations is a coupling term between both species: solar wind protons and cometary ions, which we assume to be H_2O^+ ions. This term allows the solar wind flow to get *mass loaded* with cometary ions as they diffuse upwards from the tail, and cometary ions to be accelerated by the fast, streaming solar wind. The coupling term is taken from the work of Szego et al (2000) who describe the treatment of mass loaded plasmas. However, in order to isolate the effects of the viscous-like forces, we do not consider the ongoing creation of new ions in the flow, by photoionization or any other mechanism, as is usually done in mass loading studies. Considering that we are modelling only the flow in and around the tail of the comet, the only source of additional ions in our problem is through the boundary condition at the left hand edge of our simulation box (see §2.3). It is clear that the 2D character of our simulations is an approximation to the real problem and may not allow us to study some processes that may be essential for the dynamical evolution of the flow. We make this approximation considering that this is the first approach to the problem in which viscous-like forces are taken into account. We also neglect the effect of the IMF entrained in the solar wind flow, and leave for future work the study of the dynamical effects of $\mathbf{J} \times \mathbf{B}$ forces, although we do not expect these to be dominant in the region (see arguments in the Introduction section).

Since we are interested in the gas dynamics in the tail we focus on the region behind the coma, starting from a few times 10^4 km behind the comet's nucleus and extending downstream to a few times 10^5 km as illustrated in Figure 1.

2.1. Basic equations

The present code solves the Euler equations for mass, momentum and energy conservation, including terms representing the viscous-like effects and interspecies coupling due to turbulence and/or wave-particle interactions. In Cartesian coordinates and in conservative form, for species a , these can be written as:

$$\frac{\partial \mathbf{U}^a}{\partial t} + \frac{\partial \mathbf{E}^a}{\partial x} + \frac{\partial \mathbf{F}^a}{\partial y} = \mathbf{S}^{ab} \quad (1)$$

where

$$\mathbf{U}^a = \begin{pmatrix} \rho^a \\ \rho^a V_x^a \\ \rho^a V_y^a \\ E_t^a \end{pmatrix}, \quad (2)$$

$$\mathbf{E}^a = \begin{pmatrix} \rho^a V_x^a \\ \rho^a V_x^a V_x^a + k_1^a p^a - k_2^a T_{xx}^a \\ \rho^a V_x^a V_y^a - k_2^a T_{xy}^a \\ (E_t^a + k_3^a p^a) V_x^a - k_4^a (V_x^a T_{xx}^a + V_y^a T_{xy}^a) + k_5^a q_x^a \end{pmatrix}, \quad (3)$$

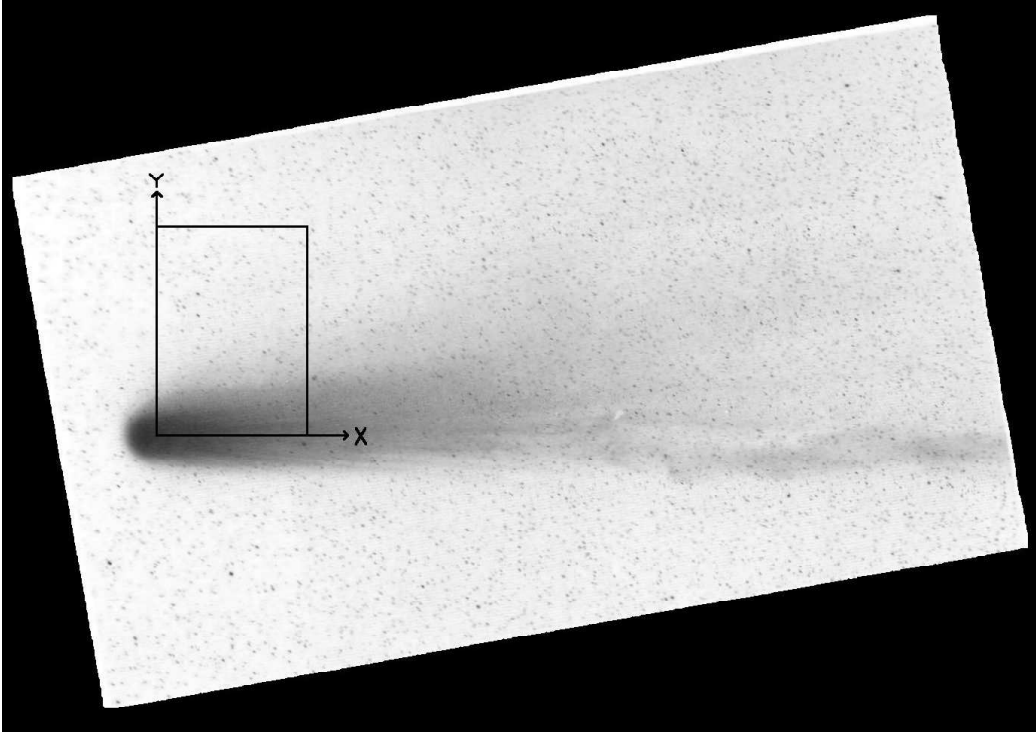


Fig. 1. Illustration of the computational domain we use for our simulations. The box provides an approximate scale of the simulated region. Image of comet Halley taken the day of the encounter with Giotto by F.Miller, University of Michigan/CTIO (Brandt et al. 1992).

$$\mathbf{F}^a = \begin{pmatrix} \rho^a V_y^a \\ \rho^a V_x^a V_y^a - k_2^a T_{xy}^a \\ \rho^a V_y^a V_y^a + k_1^a p^a - k_2^a T_{yy}^a \\ (E_t^a + k_3^a p^a) V_y^a - k_4^a (V_x^a T_{xy}^a + V_y^a T_{yy}^a) + k_5^a \dot{q}_y^a \end{pmatrix}, \quad (4)$$

and the inter-species coupling term

$$\mathbf{S}^{ab} = \begin{pmatrix} 0 \\ \rho^a \nu_{ab} (V_x^a - V_x^b) \\ \rho^a \nu_{ab} (V_y^a - V_y^b) \\ \frac{3}{2} k_3^a \rho^a \nu_{ab} [T^b - T^a] + \frac{k_3^a}{k_1^a} \rho^a \nu_{ab} [\mathbf{V}^b - \mathbf{V}^a]^2 \end{pmatrix}. \quad (5)$$

In the preceding equations ρ^a is the mass density of gas a , V_x^a and V_y^a are its velocity components, T^a is its temperature and E_t^a is the total energy density of species a defined by;

It is important to point out that this form of the interspecies coupling term, although widely used in multispecies gas modelling in various astrophysical scenarios (e.g. Schunk & Nagy, 1980, Draine, 1986, Cravens, 1991, Falle, 2003, Van Loo et al. 2009, Szego et al. 2000 and references therein), can be derived strictly from the Boltzmann collision integral only for the case corresponding to Maxwell molecules (see for example Gombosi, 1994). We use it for lack of a similarly simple, alternative expression for charged particles, and must be considered an approximation of uncertain validity in our case. Schunk (1977) has discussed the modifications to these expressions for interspecies coupling for electrically charged molecules and in future contributions we shall explore the effect of such modifications. In the present calculations we have chosen this approach to modelling multispecies flow, which follows the dynamics of each species separately, instead

of an approach following a single fluid, composed of many different species, in order to clearly disentangle the widely different properties (ρ , \mathbf{V} , T , etc) of solar wind and cometary ions.

The coupling between species represented by the term \mathbf{S}^{ab} in equation (1) is taken from the work of Szego et al (2000), and has the form of the traditional coupling resulting from binary collisions. The term ν_{ab} contained in \mathbf{S}^{ab} , reflects the effective result of all processes able to transfer momentum and energy from one species to another. Note that in the adimensional form of the equations ν_{ab} is actually $t_o \nu_{ab}$, that can be viewed as the ratio of the flow crossing time, $t_o = L/V_o$, to the inter-species coupling timescale, $1/\nu_{ab}$. In order to preserve the symmetry between the coupling terms for both species, guaranteed by the identity $\rho^a \nu_{ab} = \rho^b \nu_{ba}$, we scale ν_{ab} as ρ^b and ν_{ba} as ρ^a with a single proportionality constant, ν_o , which we take as uniform and constant. In our present code, ν_o enters as a parameter that can be varied to compare the importance of inter-species coupling to viscous-like forces.

$$E_t^a = \rho^a e^a + \frac{1}{2} \rho^a (V^a)^2 \quad (6)$$

with e^a being the internal energy per unit mass. In equations (3) and (4), the coefficients k_i^a ($i = 1, 5$) are the following combinations of dimensionless numbers and the adiabatic index for the gas, γ^a :

$$k_1^a = \frac{1}{\gamma^a M_o^2}, \quad (7)$$

$$k_2^a = \frac{1}{R_{\text{eff}}^a}, \quad (8)$$

$$k_3^a = (\gamma^a - 1), \quad (9)$$

$$k_4^a = \frac{\gamma^a (\gamma^a - 1) M_o^2}{R_{\text{eff}}^a}, \quad (10)$$

$$k_5^a = \frac{\gamma^a}{R_{\text{eff}}^a P r^a}, \quad (11)$$

where the Mach number (M_o), the Reynolds number (R_{eff}^a) and Prandtl number ($P r^a$) for the flow of gas a , are defined respectively as:

$$M_o = \frac{V_o}{C_{so}}, \quad (12)$$

$$R_{\text{eff}}^a = \frac{\rho_o V_o L}{\mu_o^a}, \quad (13)$$

$$P r^a = \frac{\mu_o^a c_p^a}{\kappa_o^a}. \quad (14)$$

Quantities with subindex o are those used for the normalization of the flow variables and parameters, the reference sound speed is defined as $C_{so} = \sqrt{\gamma^a P_o / \rho_o}$, c_p^a is the specific heat at constant pressure for gas a , and L is the normalization for the spatial coordinates. For simplicity we have assumed that the flow parameters, μ and κ , are uniform and that $\mu^a = \mu_o^a$, $\kappa^a = \kappa_o^a$, $\mu^b = \mu_o^b$ and $\kappa^b = \kappa_o^b$.

The terms T_{xx}^a , T_{xy}^a and T_{yy}^a in equations (3) and (4) represent the components of the viscous-like stress tensor given by:

$$T_{xx}^a = \frac{4}{3} \frac{\partial V_x^a}{\partial x} - \frac{2}{3} \frac{\partial V_y^a}{\partial y}, \quad (15)$$

$$T_{xy}^a = \frac{\partial V_y^a}{\partial x} + \frac{\partial V_x^a}{\partial y}, \quad (16)$$

and

$$T_{yy}^a = -\frac{2}{3} \frac{\partial V_x^a}{\partial x} + \frac{4}{3} \frac{\partial V_y^a}{\partial y}. \quad (17)$$

As is done in multiple fluid dynamics applications (Lesieur, 1990), we use the Boussinesq hypothesis in writing the Reynolds stress tensor, i.e. we adopt a “standard” form for the relation between the viscous-like stress tensor and the large scale flow velocity, using an effective viscosity coefficient that encapsulates turbulent viscosity as well as the possible effect of wave-particle interactions (Shapiro et al. 1995) or any other plasma instabilities leading to an increased coupling between ions in these collisionless plasmas.

Also, in equations (3) and (4), \dot{q}_x^a and \dot{q}_y^a are the components of the effective heat flux vector for species a (under the Boussinesq hypothesis):

$$\dot{q}_x^a = -\frac{\partial T^a}{\partial x}, \quad (18)$$

and

$$\dot{q}_y^a = -\frac{\partial T^a}{\partial y}. \quad (19)$$

Furthermore, we have assumed throughout this work that both gases are ideal so that:

$$e^a = \frac{1}{\gamma^a - 1} \frac{p^a}{\rho^a}, \quad (20)$$

with the equation of state, $p^a = \rho^a RT^a$. We have assumed that both the solar wind plasma and the cometary plasma, in the tail region, are characterized by an adiabatic index, $\gamma^a = \gamma^b = 5/3$. In the section 4 of the paper we present some results for $\gamma^b = 1.25$, and discuss the effects of changing this property of the cometary plasma.

An analogous set of equations and definitions are written for species b , and both set of equations, coupled by the source term S^{ab} in equation (1), are solved simultaneously.

2.2. Numerical code

The set of equations described above is discretized in space using 2nd order finite differences, and is advanced in time using an explicit, 2nd order MacCormack scheme (Anderson 1995). The implementation of the scheme is an extension of that described in Reyes-Ruiz et al. (2008), but now with the additional source term S in the equations of motion. In MacCormack’s scheme the solution is advanced over one timestep by a sequence of intermediate steps, the predictor and corrector steps. In the predictor step an intermediate solution (U^*) is calculated from the values of the physical variables, $U_{i,j}^t$, at a given time, t , and position, (x_i, y_j) , according to:

$$U_{i,j}^* = U_{i,j}^t - c_1 [E_{i+1,j}^t - E_{i,j}^t] - c_2 [F_{i,j+1}^t - F_{i,j}^t] + \Delta t S_{i,j}^t \quad (21)$$

where $c_1 = \Delta t / \Delta x$, $c_2 = \Delta t / \Delta y$ and E^t , F^t and S^t are evaluated with U^t according to (3), (4) and (5). This predicted solution is then corrected to obtain the solution at the next time, $t + \Delta t$, using:

$$\begin{aligned} \mathbf{U}_{i,j}^{t+\Delta t} = & \frac{1}{2} \left[\mathbf{U}_{i,j}^t + \mathbf{U}_{i,j}^* - c_1 (\mathbf{E}_{i,j}^* - \mathbf{E}_{i-1,j}^*) \right. \\ & \left. - c_2 (\mathbf{F}_{i,j}^* - \mathbf{F}_{i,j-1}^*) + \Delta t \mathbf{S}_{i,j}^* \right] \end{aligned} \quad (22)$$

where \mathbf{E}^* , \mathbf{F}^* and \mathbf{S}^* are computed from \mathbf{U}^* using (3), (4) and (5). Further details of the implementation of MacCormack's scheme are given in Reyes-Ruiz et al. (2008).

A final upgrade to our previous code is the ability to handle some types of non-uniform, cartesian grids. For the simulations done in this work, the grid is defined by a series of (x_i, y_j) coordinates for which the spacing is arbitrary. In our simulations the x_i points are geometrically distributed from x_{min} to x_{max} with nx elements. The y_j points are equispaced at the initial location of the tail (from $y = 0$ to $y = 1$ having 30 gridpoints) and geometrically distributed from $y = 1$ to $y = y_{max}$. In both series the common ratio is 1.02. The 2nd order approximation for the x -derivative of a function f at x_i can be easily obtained from the Taylor series expansion of the function at x_{i-1} and x_{i+1} , and is given by:

$$\left(\frac{df}{dx} \right)_i = \frac{\Delta x_{i-1}^2 f_{i+1} + [\Delta x_i^2 - \Delta x_{i-1}^2] f_i - \Delta x_i^2 f_{i-1}}{[\Delta x_{i-1} \Delta x_i^2 - \Delta x_i \Delta x_{i-1}^2]}$$

where $\Delta x_i = x_{i+1} - x_i$. An analogous expression exists for the y -derivative. This grid allows a higher resolution in the vicinity of the region of strong interaction, while putting the $y = y_{max}$ boundary sufficiently far to avoid numerical artifacts in our results.

2.3. Initial and boundary conditions

The solution for the flow is evolved from the following initial conditions. A dense, cold, slow moving plasma representing the tail is located between $y = 0$ and $y = 1$. Both H_2O^+ and H^+ ions are present in the tail, but with protons much less abundant than H_2O^+ . Between $y = 1.5$ and $y = y_{max}$, the gas has the properties of a shocked, hot, fast moving solar wind that contains both H_2O^+ and H^+ ions, with the number density of protons 50 times greater than H_2O^+ . In all the calculations presented here, we have adopted a value $M_o = 2$ for the Mach number of the shocked solar wind incident on our computational domain. This assumption is made based on the results of Spreiter & Stahara (1980) who computed the the gas dynamics of the flow of the shocked solar wind in the ionosheath of Venus. Spreiter & Stahara (1980) found that the flow is characterized by $M = 2$, as the solar wind crosses the terminator of the planet (the line separating the day and night sides) and heads tailwards. In comets, we take the terminator to coincide approximately with the location of the nucleus. Between $y = 1.0$ and $y = 1.5$ there is transition region where the flow properties change smoothly in an exponential manner from those in the tail to those in the solar wind. The initial density of each species is taken to be:

$$\rho^a(t=0) = \begin{cases} 0.025 \rho_{\text{tail}} & \text{if } y < 1 \\ \rho_{\text{sw}} & \text{if } y > 1.5 \end{cases}, \quad (23)$$

$$\rho^b(t=0) = \begin{cases} \rho_{\text{tail}} & \text{if } y < 1 \\ 0.32 \rho_{\text{sw}} & \text{if } y > 1.5 \end{cases}. \quad (24)$$

We assume both species are moving initially with the same velocity:

$$V_x^{a,b}(t=0) = \begin{cases} V_{\text{tail}} & \text{if } y < 1 \\ V_{\text{sw}} & \text{if } y > 1.5 \end{cases}, \quad (25)$$

$$V_y^{a,b}(t=0) = 0. \quad (26)$$

In normalized quantities $V_{\text{sw}} = 1$ and $V_{\text{tail}} = 0.01$. For the results shown here we use, in normalized variables, $\rho_{\text{sw}} = 1$ and $\rho_{\text{tail}} = 400$. The local temperature of both species is assumed the same inside the tail, with $T_{\text{tail}}^a = T_{\text{tail}}^b = T_{\text{tail}}$ and $T_{\text{sw}} = 100T_{\text{tail}}$, with $T_{\text{sw}} = 1$ in normalized units. Outside the tail, for $y > 1.5$, cometary ions are injected with a temperature an order of magnitude lower than the streaming solar wind protons, $T_{\text{sw}}^a = 10T_{\text{sw}}^b = T_{\text{sw}}$. This choice of temperatures and densities is made to yield an initial pressure balance between the H_2O^+ plasma (species b) inside the tail, and the proton plasma (solar wind, species a) outside. With $p^a = \rho^a T^a$ and $p^b = (m_p^a/m_p^b)\rho^b T^b$, m_p^a and m_p^b being the particle mass for species a and b respectively, we find that our choice of initial conditions is characterized by a pressure in-balance among each species. Whether the rapid movement of cometary ions resulting from this initial condition is prevented by the wrapped-around IMF over the comet's tail will be the subject of future studies. Although significantly different from the flow properties at later times in the simulations, for all the cases we have studied these initial conditions do not give rise to any long lasting instability in the flow so that the final state does not depend on their precise form or value.

The boundary conditions are chosen to be consistent with the initial conditions. At the left boundary, $x = x_{\text{min}}$, the flow density and velocity follow exactly that given by the initial condition in equations (23)-(26). Considering that the inflow to the comet's tail ($y < 1$) is subsonic, we allow the inflow pressure to float freely as a linear extrapolation of the active mesh values (e.g. Anderson 1995). The right side boundary, $x = x_{\text{max}}$, corresponds to the commonly used outflow conditions for supersonic flows, namely the derivatives being zero for all flow variables. We have also run simulations with an outer boundary condition obtained from linearly extrapolating the flow variables, resulting only in minor differences in the last gridpoints before the $x = x_{\text{max}}$ boundary.

3. Results

We have performed a series of simulations with different set of parameters $R_{\text{eff}}^{a,b}$ and v_o to determine the effect of viscous forces and inter-species coupling in the flow dynamics. For all cases considered, the flow evolves from the prescribed initial condition [eqns. (23)-(26)], passing through a fast transient phase, during which a considerable portion of the mass originally in the tail is eroded by the solar wind exiting our simulation domain. The relevance of this transient phase, lasting a few tens of solar wind crossing times ($t_o = L/V_o$), in relation to observed features in the evolution of the ion tail, will be analysed in a future publication. In this work we concentrate on the following, quiescent stage of evolution since, given its longer timescale for existence, is more likely to be encountered. In all cases, we present results for the flow velocity, density and temperature after a time long enough that a quasi-steady state has been reached. All results are presented in terms of normalized quantities as defined in the previous section. For a particular application, appropriate values of L , V_o , ρ_o and T_o can be chosen as exemplified in Section 4 for comet Halley.

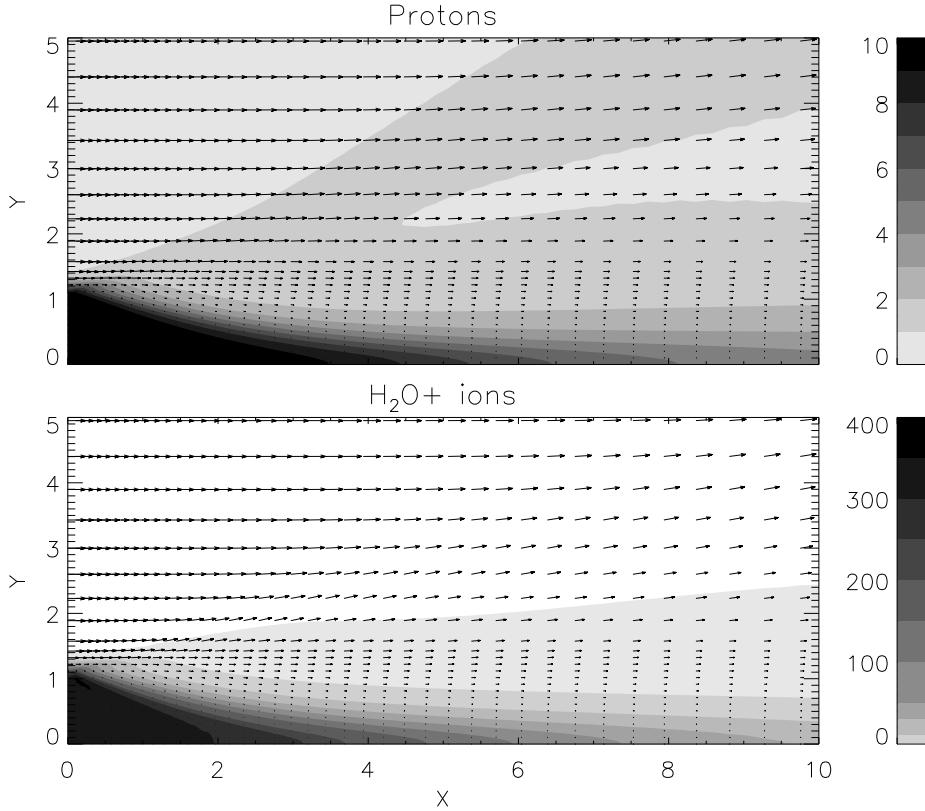


Fig. 2. Density contours (shades of gray) and flow geometry (velocity vectors) for Case 1 ($Re^{a,b} = 30$, $v_o = 0.1$) after 1234 simulation time units. The top panel shows the configuration for the proton plasma (species a) and the right side panel shows the “equilibrium” configuration for cometary H_2O+ ions. Density and velocity are in normalized units.

To determine the appropriate value of the effective Reynolds number for each species we consider the following. According to Perez-de-Tejada (1989) the geometry of the flow, measured *in situ* by the Giotto spacecraft in its fly-by comet Halley in march 1986, implies an effective Reynolds number around 350 for the shocked solar wind flow above the cometopause along the spacecraft trajectory. In contrast, in a similar region in the ionosheath of Venus, Perez-de-Tejada (1999) and Reyes-Ruiz et al (2008) estimate a value of the Reynolds number an order of magnitude smaller ($R_{eff} = 20$), based on a comparison of *in situ* measurements (by the Venera 10 and Mariner 5 spacecraft) at Venus with the flow properties derived from a numerical simulation of the viscous-like solar wind-ionosphere interaction. To assess the estimation of Perez-de-Tejada (1989) we have conducted simulations with 3 different values of the Reynolds number. A high value, $R_{eff} = 100$, similar to that estimated by Perez-de-Tejada (1989) for comet Halley; an intermediate value, $R_{eff} = 30$, comparable to the value estimated by Reyes-Ruiz et al. (2008) for the solar wind flow in the ionosheath of Venus; and a low value, $R_{eff} = 10$, used to verify the tendency in the results as R_{eff} is decreased.

In most cases, the value of the effective Reynolds number for both species is assumed to be the same, In our view, the lack of knowledge of the precise mechanisms giving rise to the effective vis-

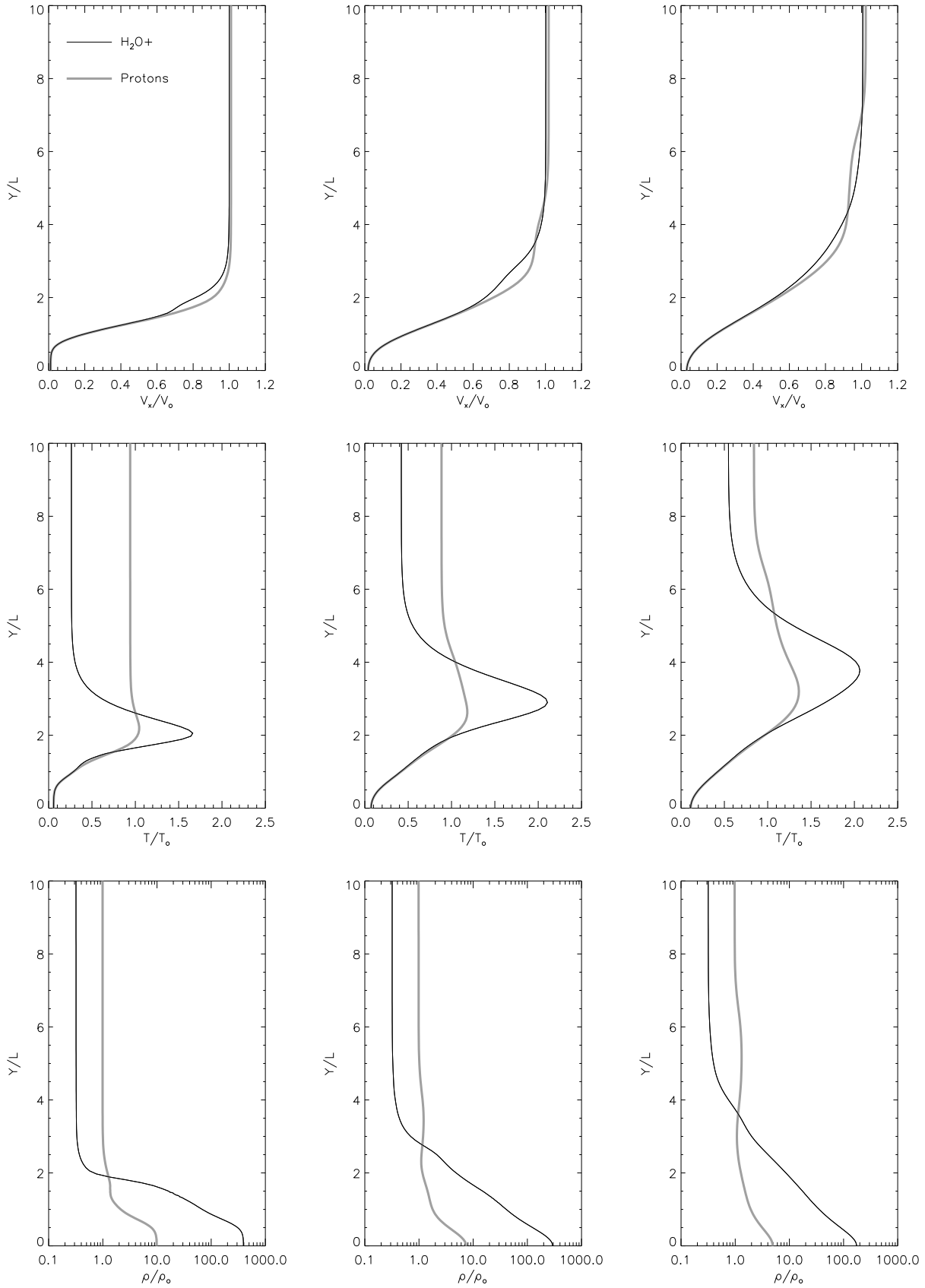


Fig. 3. Vertical profiles of the flow properties for Case 1 at three different positions; $x = 2$ (left column of panels), $x = 5$ (middle column) and $x = 8$ (right column). In all cases, gray lines indicate the properties of the proton plasma (species a) and black lines denote the properties of the H_2O^+ plasma (species b). The top row shows the x component of velocity, $V_x^{a,b}$, the middle row shows the temperature, $T^{a,b}$, and the bottom row shows the mass density, $\rho^{a,b}$. All quantities are in

cosity in these plasmas justifies this assumption. However, we have analysed a case with different values of the effective Reynolds number for each species in the Discussion section.

The value of ν_o is also varied to explore the relative importance of inter-species coupling, *versus* viscous forces, which are proportional to $R_{\text{eff}}^{a,b}$. We will show results for 3 different cases: a strong coupling case characterized by $\nu_o = 1$, which can be interpreted as having the timescale for inter-species coupling equal to the solar wind crossing timescale, $t_o = L/V_o$; a medium coupling case, in which the coupling timescale is an order of magnitude greater than the crossing timescale, $\nu_o = 0.1$; and a weak coupling case, for which $\nu_o = 0.01$, so that inter-species coupling effects are much smaller than other dynamical effects.

To compare the state of the flow at the same time in its evolution for all cases, starting from the same initial condition, we have chosen, arbitrarily, to show results at $t = 1234$, with time units in multiples of the solar wind crossing time. The number of timesteps required to reach this time depends on the model parameters, for most cases less than 200 000 timesteps are required.

3.1. Effect of inter-species coupling

Our fiducial model, Case 1, is characterized by model parameters $R_{\text{eff}}^{a,b} = 30$ and $\nu_o = 0.1$. In Figure 2 we show density contours and the flow velocity for each species. Initially the tail contained a uniform density, $\rho^a = 10$ (protons) and $\rho^b = 400$ (H_2O^+ ions) for $y < 1$, and after $t = 1234 t_o$, a significant portion of the tail has been eroded by the effect of viscous forces and inter-species coupling. A shock wave is evident in the deflection of the flow velocity from the initial uniform distribution imposed by the boundary condition at $x = x_{\text{min}}$. Also noticeable is the strong velocity gradient around $y = 2$ which corresponds to the viscous boundary layer. Both effects are also shown in Figure 3, where vertical profiles of the x component of velocity, V_x , temperature, T , and mass density, ρ , are shown for three different x -positions, $x = 2, 5$ and 8 ; in the left, middle and right columns of each figure, respectively.

In Figure 3 the shock front and the boundary layer can be identified at all 3 positions, but they are well separated only for $x = 5$ and $x = 8$, shown in the middle and right hand columns, respectively. For a given V_x profile, the shock front corresponds to the uppermost decrease from the uniform velocity ($V_x = 1$) in the free flowing solar wind. In the middle panel, corresponding to $x = 5$, this transition is located approximately at $y = 5$. A second transition, located approximately at $y = 2.5$ for $x = 5$, marks the top of the viscous boundary layer, below which the velocity drops sharply to the very low flow velocities in the middle of the tail. The shock front can also be seen as an increase in both temperature and density in the corresponding panels for each position. The temperature increase and density decrease characteristic of viscous boundary layers and found in previous studies of viscous flow over a flat plate (e.g. Reyes-Ruiz et al. 2008), is also observed in other cases modeled here. This clearly indicates that the region around $y = 2$ (at $x = 5$) is indeed a viscous boundary layer.

For Case 2 we use the same Reynolds number, $R_{\text{eff}}^{a,b} = 30$, as in Case 1, but increase the importance of inter-species coupling by using $\nu_o = 1.0$. A Figure showing the general flow geometry is not shown since no appreciable differences are found with Case 1 (shown in Figure 2). However, the vertical profiles of flow properties, shown in Figure 4, clearly illustrate the effect of a much stronger inter-species coupling used in this model. Namely, as both species are more tightly coupled, their

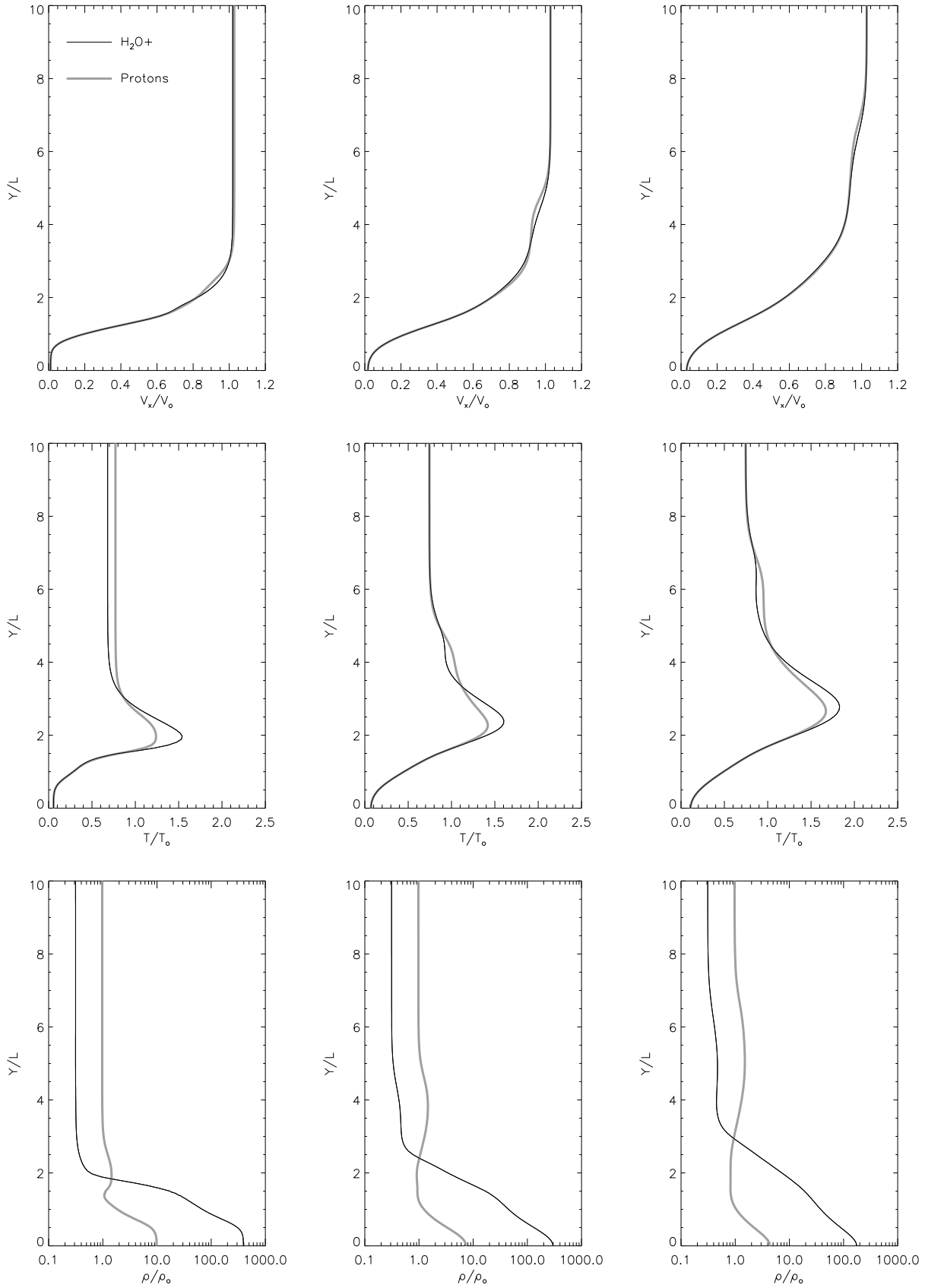


Fig. 4. Same as in Figure 3 but for simulation Case 2 ($R_{\text{eff}}^{a,b} = 30$, $v_o = 1.0$).

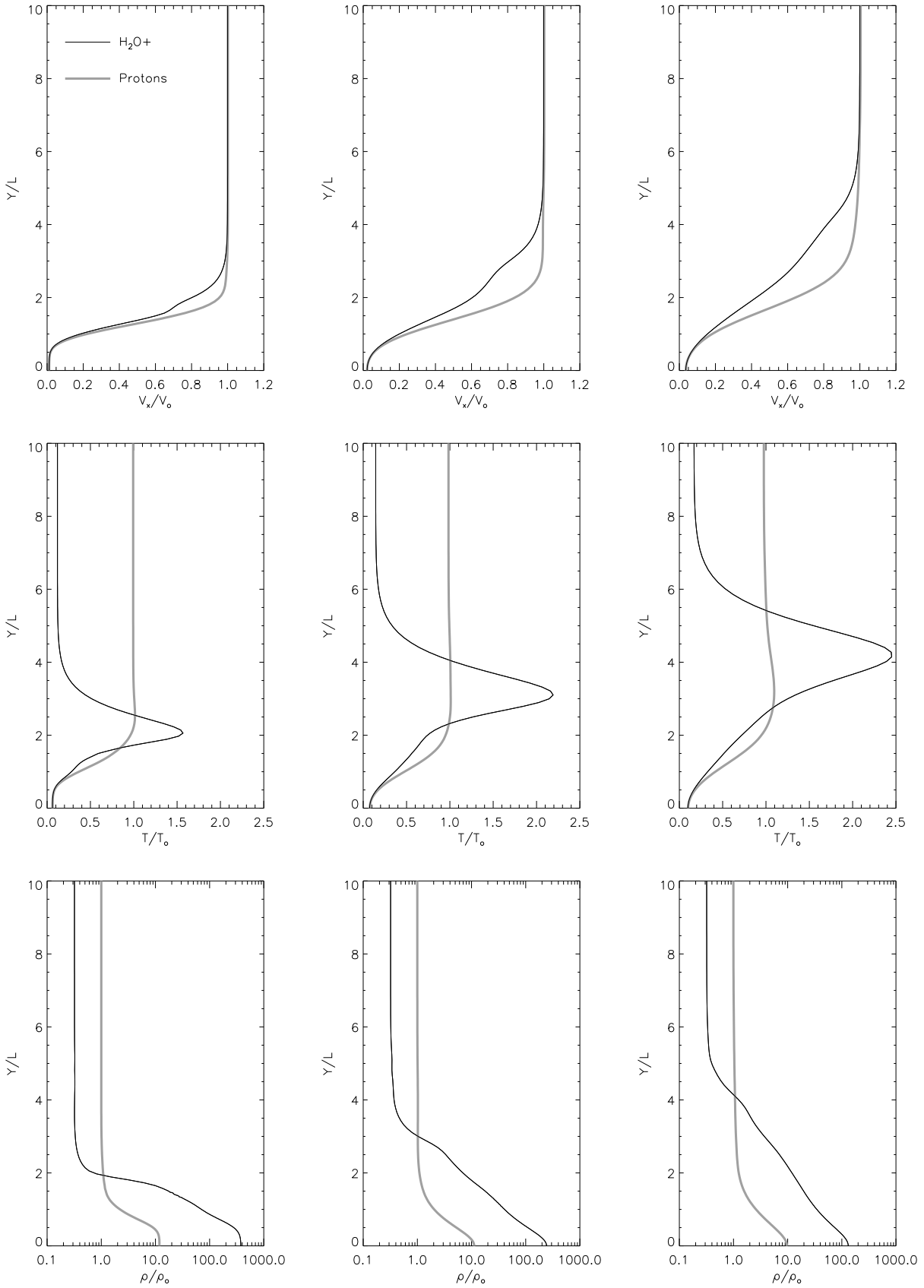


Fig. 5. Same as in Figure 3 but for simulation Case 3 ($R_{\text{eff}}^{a,b} = 30$, $\nu_o = 0.01$).

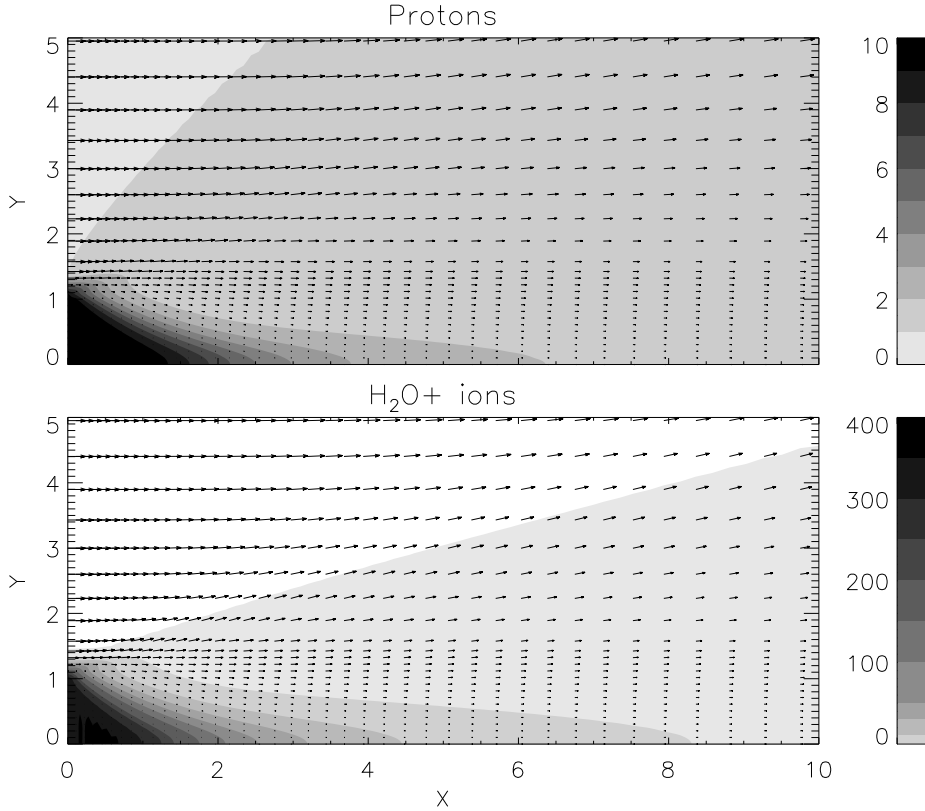


Fig. 6. Same as in Figure 2 but for simulation Case 4 ($R_{\text{eff}}^{a,b} = 10$, $\nu_o = 0.1$).

velocity and temperature distribution tend to be almost identical. The density distribution conforms to the different boundary conditions for each species, since these are different, there is no reason why both densities should tend to equalize and they do not. Figure 4 shows that the shock front and the boundary layer are not well separated at the rightmost position shown, $x = 2$. From the shock front height and boundary layer thickness shown in the middle and right columns of Figure 4, we see that both are proportional to the inter-species coupling (see §4). The shock front height at $x = 5$, for example, changes from $y = 4.7$ for Case 1, to $y = 5.5$ in this case, while the thickness of the boundary layer goes from $y = 2.8$ to $y = 3.2$ as we increase the inter-species coupling parameter from 0.1 to 1.

In Figure 5 we show the results for Case 3 characterized by a very weak inter-species coupling, $\nu_o = 0.01$. The general flow geometry (not shown) is very similar to that in Figure 2. A comparison of Figure 5 (weak coupling) with Figures 3 and 4 (medium and strong coupling respectively), clearly shows that in Case 3 the dynamics of both species is essentially uncoupled. The location of the shock front and the top of the boundary layer are different for each species. For example, at $x = 5$, only for the cometary H_2O^+ ions the shock front and boundary layer are clearly separated. For the H_2O^+ ions the shock front is located approximately at $y = 5$ and the top of the boundary layer is at $y = 2.5$, while for protons the shock front and the top of the boundary layer are both located around $y = 2$.

3.2. Effect of viscous-like forces

To analyse the effect of the viscous-like momentum transport between the solar wind and material in the comet's plasma tail, we compare 3 simulations with the same inter-species coupling parameter, $\nu_o = 0.1$, but different values of the effective Reynolds number. Figures 6 and 7 show the resulting flow geometry and vertical profiles, respectively, for our Case 4, characterized by a higher viscosity corresponding to a lower effective Reynolds number, $R_{\text{eff}} = 10$, than Case 1. Comparing the global geometry of the flow in this case (Figure 6) with that in a case with greater Reynolds number, $R_{\text{eff}}^{a,b} = 30$ (Figure 2) we see that after 1234 crossing times, the erosion of the tail is much greater in this high viscosity case for both species. This result is expected as well as the increase in the thickness of the boundary layer as we decrease the effective Reynolds number. This is clearly seen when comparing the vertical profiles of the flow properties shown in Figure 3 (medium viscosity) and Figure 7 (high viscosity). For example, as shown in Figure 7 for $x = 5$, the top of the boundary layer increases from $y = 2.8$ for $Re^{a,b} = 30$ to approximately $y = 3.7$ for $R_{\text{eff}}^{a,b} = 10$. The increased thickness of the boundary layer as we decrease $R_{\text{eff}}^{a,b}$, effectively represents a more blunt obstacle to the solar wind flow. Hence, the height of the boundary layer also increases as we decrease $Re^{a,b}$. This is also shown in Figure 7 where, for example at $x = 5$, the height of the shock front is located approximately at $y = 7$; about 2 scale units higher than the shock front location for the model with lower effective viscosity (Figure 3).

The tendency seen in going from high ($R_{\text{eff}}^{a,b} = 10$) to medium effective viscosity ($R_{\text{eff}}^{a,b} = 30$) is confirmed by comparing with results with an even smaller viscosity, such as Case 5 which corresponds to a model with $Re^{a,b} = 100$, shown in Figures 8 and 9. As expected, a decreased viscosity leads to significantly less erosion of the tail than in Cases 1 and 4 (medium and high viscosity respectively) as shown in Figure 8. Also, as discussed above and as shown in Figure 9, the top of the boundary layer decreases as we increase the Reynolds number, and consequently the location of the shock front also decreases. For example, in the profiles corresponding to $x = 5$ in Figure 9, we find that the top of the boundary layer decreases from $y = 2.8$ for $R_{\text{eff}}^{a,b} = 30$ to $y = 2.2$ for $R_{\text{eff}}^{a,b} = 100$. In regards to the location of the shock front, this goes from $y = 4.8$ for $R_{\text{eff}}^{a,b} = 30$ to approximately $y = 3.7$ for $R_{\text{eff}}^{a,b} = 100$.

4. Discussion

In view of the uncertainty about the precise physical mechanisms giving rise to the effective viscosity, we have assumed that the effective Reynolds number for both species is the same in the calculations presented above. However, we have also carried out simulations having distinct effective Reynolds number for each species and find that for a medium value of the inter-species coupling, $\nu_o = 0.1$, the results are almost identical to those with a single value for the effective Reynolds number for both species (equal to the effective Reynolds number of species b). For example, for a case with $R_{\text{eff}}^a = 100$, $R_{\text{eff}}^b = 10$ and $\nu_o = 0.1$, the vertical profile of flow properties for the H_2O^+ ions at all x locations is almost identical to that shown in Figure 7 for Case 4, characterized by $R_{\text{eff}}^a = R_{\text{eff}}^b = 10$ and $\nu_o = 0.1$. The vertical profile of flow properties for the protons, while not identical, is still very similar to Case 4. This suggests that viscous stresses, particularly in the species that dominates the mass of the problem, are the dominant factor in the flow dynamics.

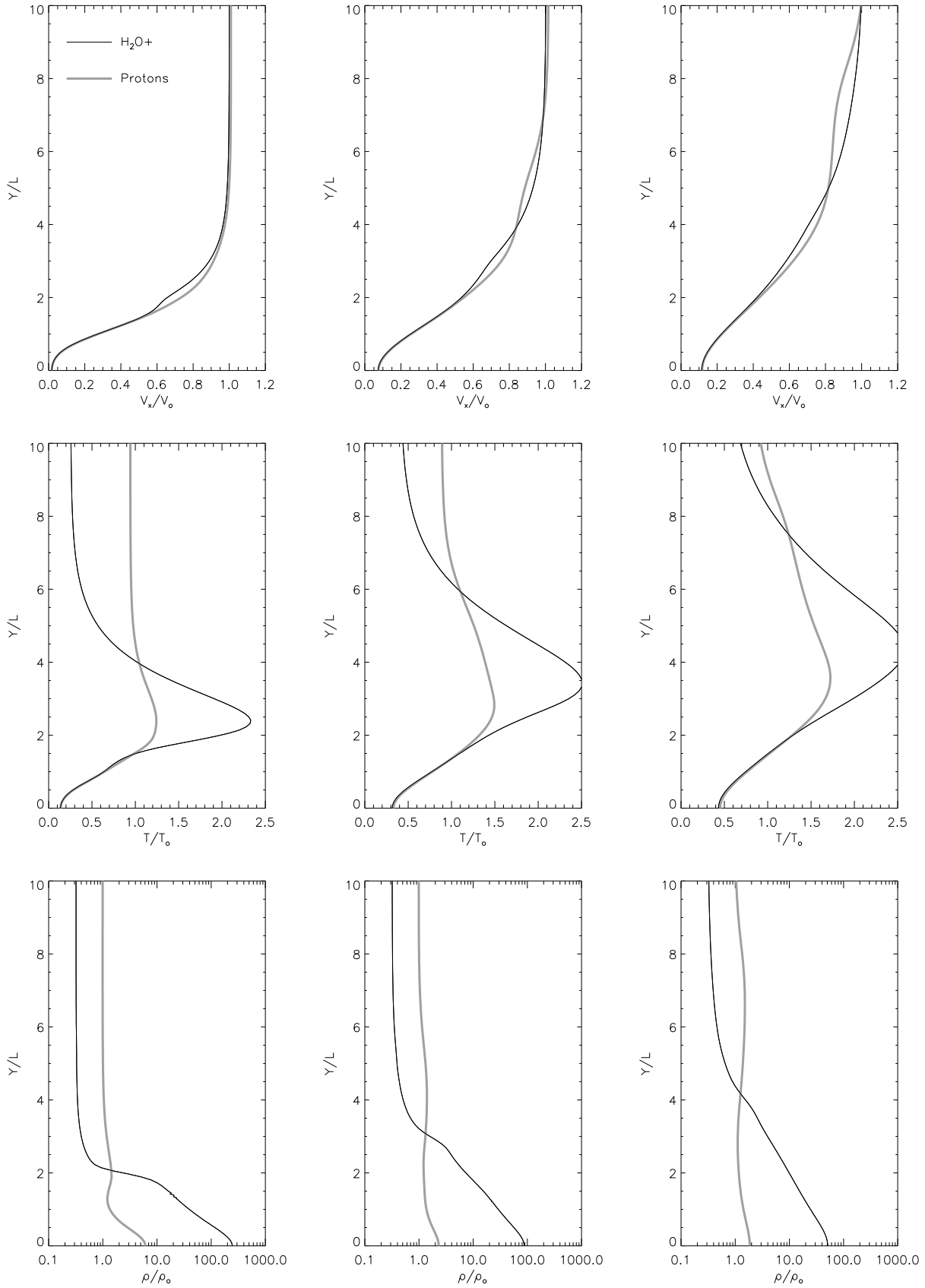


Fig. 7. Same as in Figure 3 but for simulation Case 4 ($R_{\text{eff}}^{a,b} = 10$, $\nu_o = 0.1$).

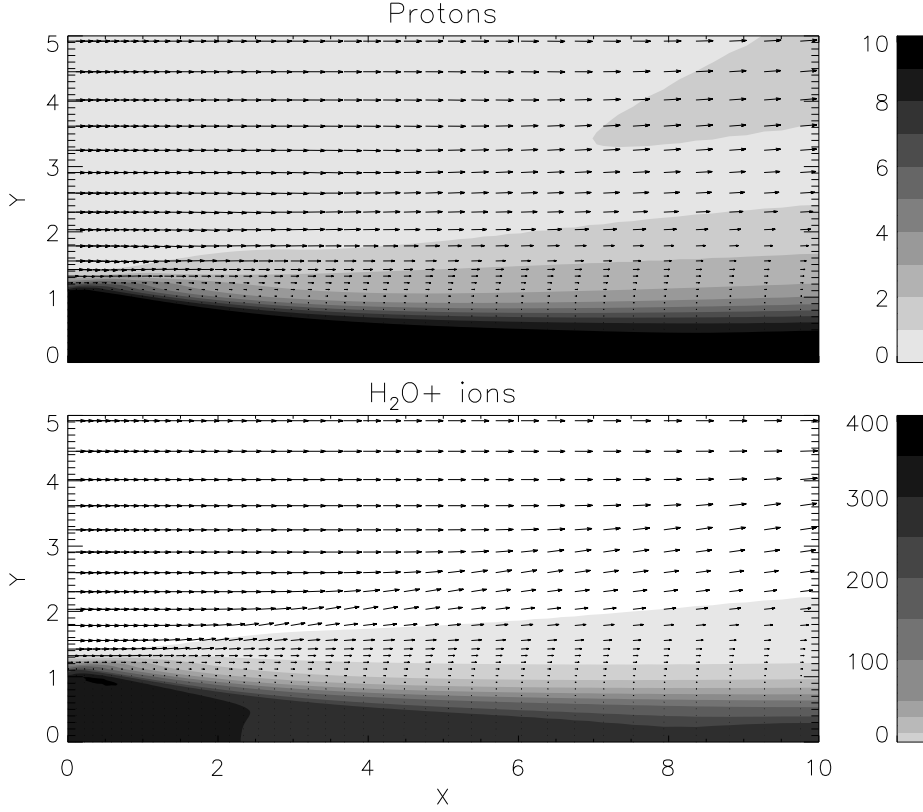


Fig. 8. Same as in Figure 2 but for simulation Case 5 ($R_{\text{eff}}^{a,b} = 100$, $\nu_o = 0.1$).

As mentioned in section 2, in the results presented above we have assumed that the adiabatic index for both species is the same, $\gamma^a = \gamma^b = 1.67$. While this value of γ can be safely assumed for the solar wind plasma (assuming thermal equilibrium for the species), it is not so clearly valid for the H_2O^+ plasma in which the excitation of rotational and vibrational degrees of freedom may lead to a lower value of γ (again assuming thermal equilibrium for the species). In order to illustrate the effect of a different, lower value of the adiabatic index for cometary plasma, we have also conducted simulations with a value $\gamma^b = 1.25$ for the adiabatic index of the H_2O^+ plasma. This value corresponds to a gas composed of triatomic molecules in thermal equilibrium at a high enough temperature for all molecular degrees of freedom to be excited. Results for this case, $\gamma^a = 1.67$ and $\gamma^b = 1.25$, with the same effective viscosity and interspecies coupling parameters as Case 1 ($R_{\text{eff}}^{a,b} = 30$ and $\nu_o = 0.1$) are shown in Figure 10 which shows the vertical profiles of V_x , T and ρ for both species in both cases.

Clearly evident when comparing Figure 10 ($\gamma^b = 1.25$) and Figure 3 ($\gamma^b = 1.67$) is the fact that if the cometary plasma is characterized by a lower value of the adiabatic index, the heating of the H_2O^+ plasma is significantly reduced in the boundary layer, since part of the dissipated energy goes to the excitation of the additional degrees of freedom corresponding to the lower value of γ . This leads to less plasma expansion in the region and a thinner velocity boundary layer. The height of the shock front is consequently reduced. In future contributions we shall address the issue of the appropriate value of γ for the cometary plasma.

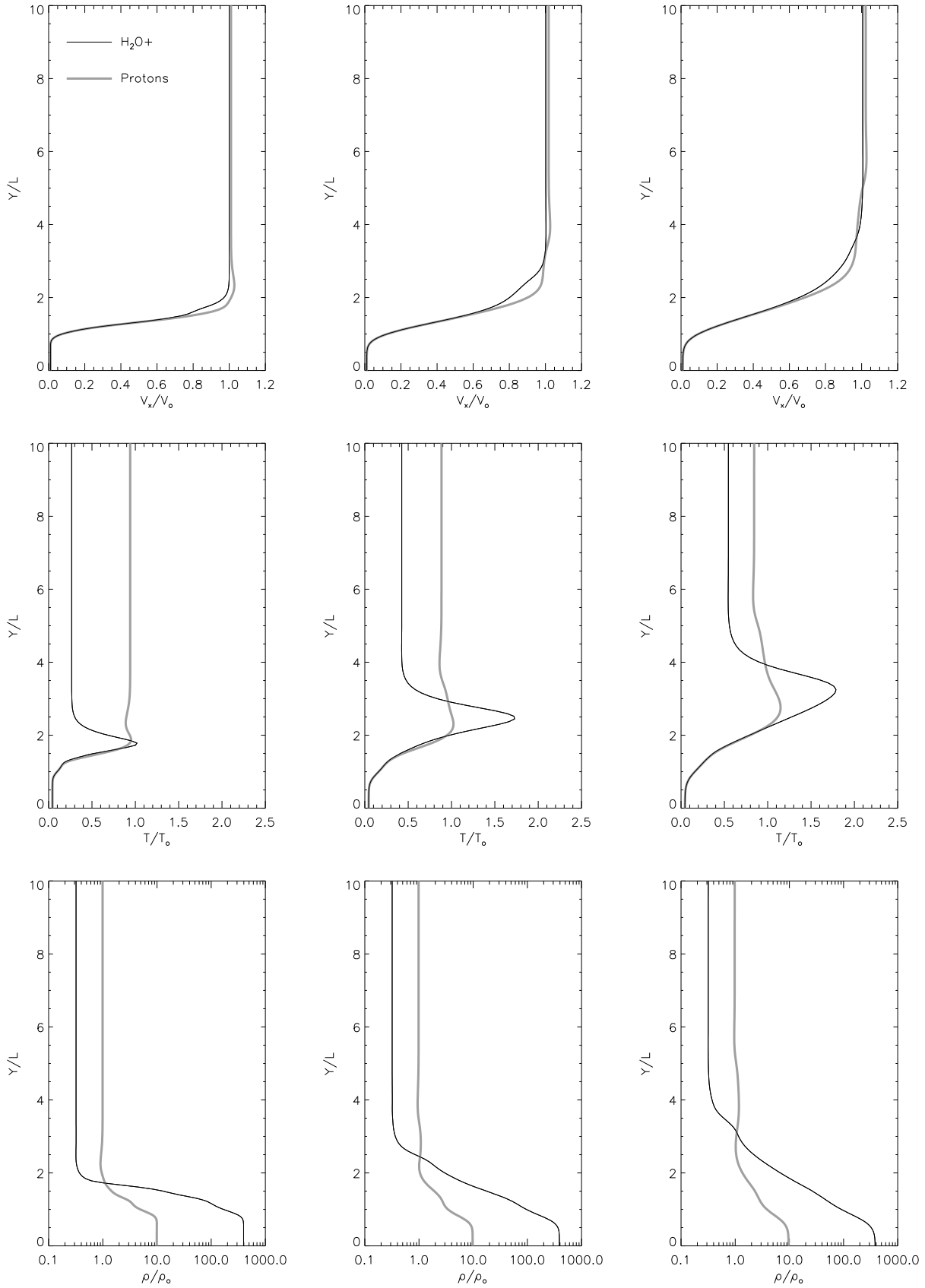


Fig. 9. Same as in Figure 3 but for simulation Case 5 ($R_{\text{eff}}^{a,b} = 100$, $v_o = 0.1$).

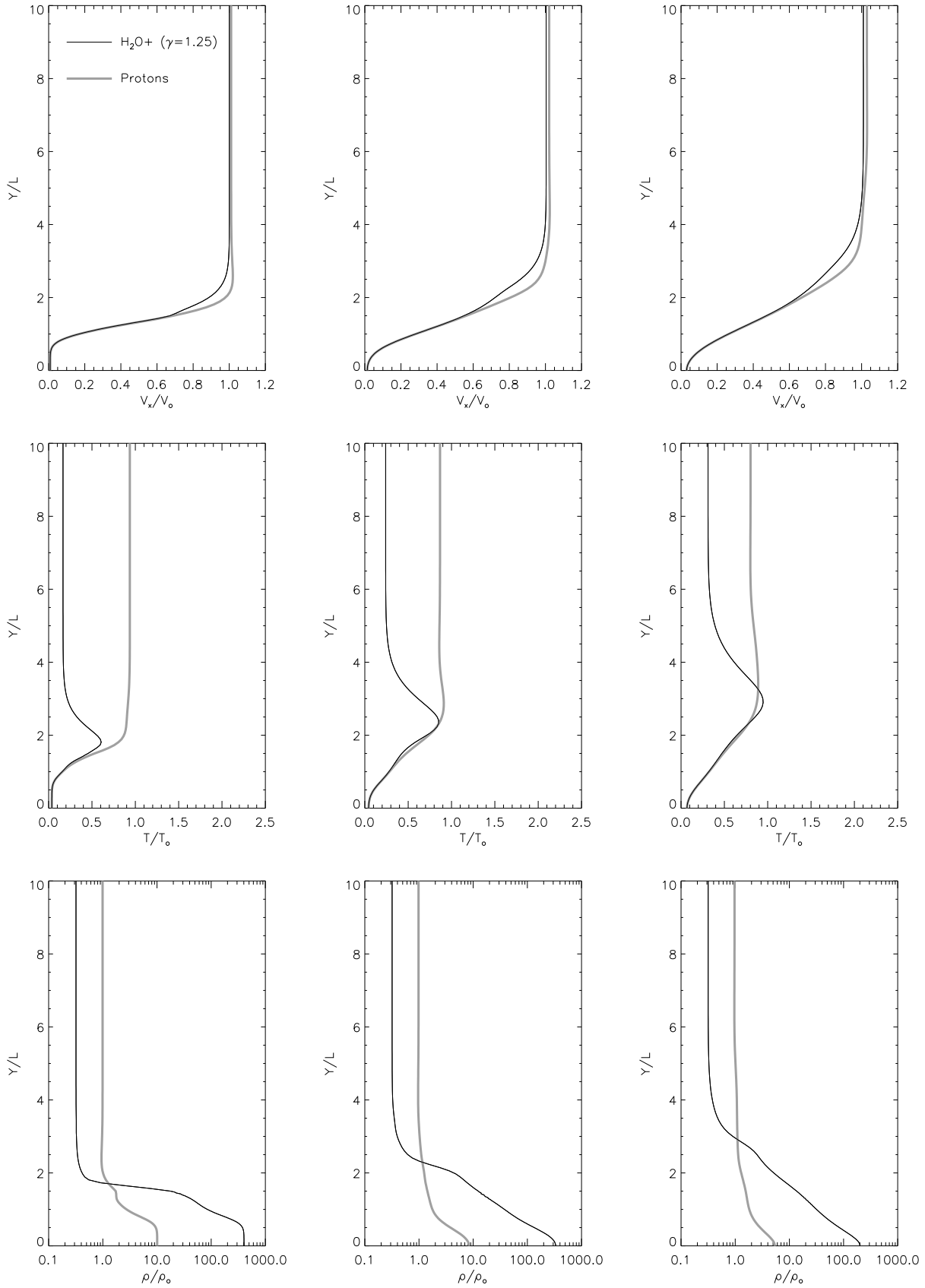


Fig. 10. Comparison of the vertical profiles of flow properties for a case characterized by the same value of R_{eff} and v_o as Case 1, but with $\gamma^b = 1.25$. Profiles at $x = 2$ (left column of panels), $x = 5$ (middle column) and $x = 8$ (right column) are shown. Gray lines indicate the properties of the proton plasma and black lines denote the properties of the H_2O^+ plasma. All quantities are in normalized units.

4.1. Comparison with *in situ* measurements

A comparison of our results with the *in situ* measurements made by the Giotto spacecraft, as it flew by comet Halley in March of 1986, is not straightforward. The simplified geometry we are using in our simulations to study the interaction in the tail region exclusively, precludes a direct comparison. Nevertheless, some insight into the implications of our results can be obtained from a simplified comparison.

Once a particular application scenario has been chosen, values for the characteristic length, velocity, density and temperature used in the adimensionalization of the equations of motion (section 2) can be established. For comet Halley, using the *in situ* measurements reported in Goldstein et al. (1986), Johnstone et al. (1986) and Perez-de-Tejada (1989), we adopt $L = 150,000$ km, $V_o = 250$ km/s, $\rho_o = 1.67 \times 10^{-23}$ gm/cm³ and $T_o = 2.5 \times 10^5$ K.

According to Johnstone et al. (1986), the Giotto spacecraft observed 3 distinct transitions in the plasma properties on its inbound trajectory towards comet Halley's nuclear region: (1) The outermost transition occurs about 900000 km from the point of closest approach and can be identified as the bow shock crossing. (2) The cometopause, where the density of cometary ions sharply increases, can be located at around 150000 km from closest approach (Perez-de-Tejada, 1989). (3) Approximately midway between the shock location and the cometopause, at about 400000 km from closest approach, the so called intermediate transition signals the top of the viscous boundary layer according to the viscous flow interpretation of the solar-wind-comet interaction given by Perez-de-Tejada (1989). Pending a more detailed comparison of the Giotto measurements with the results of our simulations, which should take into account the full geometry of the problem, let us identify the cometopause detected in the measurements with the region of very strong H₂O⁺ density increase in our simulations, located at $y = 1.0$ (approximately) in our normalized units. Under this assumption, in Figure 11 we compare the thickness of the boundary layer and the height of the shock front evaluated from our simulation results at $x = 5$, for models with different effective Reynolds number ($R_{\text{eff}}^{a,b}$) and inter-species coupling parameter (ν_o). As already seen, both the thickness of the boundary layer and the height of the shock front decrease with increasing Reynolds number so that, almost irrespective of the value of ν_o , a low value of $R_{\text{eff}}^{a,b}$ is required to explain the measured transition locations.

Also evident in Figure 11 is the dependence of the transition locations on the value of the inter-species coupling parameter. In simulations with a strong inter-species coupling, the solar wind ions are able to transfer momentum to cometary ions more efficiently giving rise to a thicker boundary layer and higher shock front. The opposite is true when both species are weakly coupled ($\nu_o = 0.01$). In such case solar wind ions flow by cometary plasma interacting very weakly. Less momentum is transferred between the solar wind and cometary plasma in a situation reminiscent of a high Reynolds number case. Our analysis of scale-heights is based not only on the properties of the velocity profiles in our simulations. As pointed out by Perez-de-Tejada (1989), there are corresponding changes in the density and temperature of the gas as one enters a boundary layer. The heating and expansion characteristic of viscous boundary layers are also found in our results, particularly for cases with low Reynolds number and high inter-species coupling parameter.

It is worth mentioning that somewhat similar properties of the flow were also measured by the ICE spacecraft in its flyby through comet Giacobinni-Zinner as discussed in Ip (2004). A com-

parison of the location of the transition from the sheath region to the so-called transition region and the bow shock location as estimated by Reme (1991), corrected for the different height of the cometopause, yields very similar relative positions to those shown by the dotted lines in Figure 11 for the transitions in comet Halley. In future work we will address the differences in the flow properties measured in comet Halley and in comet Giacobinni-Zinner.

4.2. Implications for 3D geometry

It is important to emphasize that the geometry presented in this paper is derived from a 2D model. In Venus, as discussed by Perez-de-Tejada (1995), the viscous-like interaction between solar wind and ionospheric plasmas takes place preferentially over the magnetic poles of the planet (defined in terms of the incident IMF), where the pile-up of magnetic field lines is less than around equatorial latitudes. According to Perez-de-Tejada (1995), up to about 80° SZA, the piled-up magnetic field over the dayside ionosphere and along the flanks, inhibits in some degree a direct, viscous-like interaction between solar wind and ionospheric plasmas.

If we apply these ideas to the solar wind-comet interaction, this implies that the flow properties we have computed here, correspond more closely to locations over and downstream from the magnetic poles of the comet. For different locations along the tail, the piled-up magnetic field may prevent an efficient viscous-like dragging of ionospheric material, $\mathbf{J} \times \mathbf{B}$ forces may be more important and the flow dynamics may be better modeled in terms of an MHD model as those of Wegmann (2002) and Jia et al. (2007). As the IMF is constantly changing direction on a wide range of amplitudes and timescales, the region of viscous-like interaction between the solar wind and cometary plasma, changes with time. Given the typical IMF orientation is approximately in the ecliptic plane, one should expect that the flow within $\pm 20^\circ$, measured in the y -direction (as typically defined) from the magnetic poles of the comet, is best described by our model.

5. Conclusions

We have presented results for the numerical simulation of the interaction between the solar wind and the plasma in the tail of a comet, taking into account the effect of viscous-like stresses previously argued to be important by Perez-de-Tejada et al (1980). To our knowledge, this is the first time that viscous-like effects have been incorporated into such studies. Our results indicate the existence of 3 distinct transitions in the flow properties: outermost we find a shock front, innermost we have the cometopause and an intermediate transition which we can identify with the height of the boundary layer characterized by a fast decline in the anti-sunward flow velocity, and the onset of plasma heating and expansion due to viscous-like dissipation. The location of these transitions depends on the flow parameters, namely the effective Reynolds number of the flow for each species, $R_{\text{eff}}^{a,b}$, and the inter-species coupling parameter, ν_o .

By comparing the flow properties from our numerical simulations to the location of the shock front and intermediate transition, as measured by the Giotto spacecraft as it approached the nucleus of comet Halley, we find that, almost irrespective of the strength of the inter-species coupling, ν_o ; a low value of the effective Reynolds number, approximately $R_{\text{eff}}^{a,b} \lesssim 20$ for both species, is required to reproduce the measured transition locations. This implies, in the context of our model, that the measured flow properties cannot be explained if one does not take into account the viscous-like

forces in the interaction of the solar wind and the plasma tail of a comet. Although the conclusions drawn from this study are strictly applicable only to comet Halley and solar wind conditions at the time the *in situ* measurements were taken, one may speculate that viscous-like processes may be important in the solar wind-comet interaction in general.

It is important to emphasize that, this being the first attempt to include viscous-like forces in the numerical simulation of the interaction of the solar wind with a comet's plasma environment, there are many pending issues still to be addressed that could have potentially important consequences on the details of the solutions obtained under our simplified treatment. First and foremost, the precise forms we are using for the viscous like stress and effective interspecies coupling, may be questioned. As we have argued in the Introduction, plasma properties imply that "normal" viscosity is negligible in the region under consideration. Hence, we are invoking an effective viscosity presumably resulting from plasma turbulence and/or wave-particle interactions. However, the precise form of the terms corresponding to viscous-like momentum transfer in the equations of motion (Boussinesq hypothesis) is not formally demonstrated. Also, as we have discussed in the Formulation section of the paper, the interspecies coupling terms we are using can not be strictly derived for a plasma as the one we are modelling. In view of these arguments, one may consider that the work reported in this paper is only an academic exercise of questionable applicability to the problem of solar wind-cometary plasma interaction. In such case, a similar conclusion must be reached in regards to many other studies of fluid dynamics that use similar approaches to modelling effective viscosity and interspecies coupling.

Additional important effects still to be considered are the following: geometrical effects due to the curvature of the ionosphere are required for a more direct, quantitative comparison between *in situ* measurements by the Giotto spacecraft and the results of simulations; the interaction of the charged species with neutral gas ejected from the comet which, especially in the vicinity of the nucleus, is the most abundant species; the effect of the magnetic field on the flow (particularly in the dayside and around the midplane of the near-tail region), 3D effects, incoming flow time dependence, etc. We believe that the further assessment of the relevance of these factors is beyond the present study. They are the subject of work currently in progress and will be reported in future contributions.

Acknowledgements. MRR acknowledges the support of research grant IN109409 of DGAPA-UNAM. HA acknowledges the support of research grant IN121406 of DGAPA-UNAM and CONACYT-México grant No. 508807.

References

- Alfven, H. 1957, *Tellus*, 9, 92
- Anderson, J.D. 1995, *Computational fluid dynamics : The basics with applications*, McGraw-Hill, New York
- Baker, D.N. et al. 1986, *Geophys. Res. Lett.*, 13, 271
- Bame, S.J. et al. 1986, *Science*, 232, 356
- Biermann, L. 1951, *Z. Astrophys.*, 29, 274
- Biermann, L. et al. 1967, *Sol. Phys.*, 1, 264
- Brandt, J.C. et al. 1992, *The International Halley Watch Atlas of Large-Scale Phenomena*, The University of Colorado, Boulder
- Cravens, T.E. 1991, in *Comets in the Post-Halley Era*, eds. R.L. Newburn Jr. et al., p. 1211, Kluwer Acad. Pub., The Netherlands
- Cravens, T.E. 1980, *J. Geophys. Res.*, 85, A7778

- Cravens, T.E. & Gombosi, T.I. 2004, *Advances in Space Research*, 33, 1968
- Dobe, Z. et al. 1999, *Phys. Rev. Lett.*, 83, 260
- Draine, B.T. 1986, *MNRAS*, 220, 133
- Falle, S.A.E.G. 2003, *MNRAS*, 344, 1210
- Goldstein et al. 1986, in *Proc. 20th ESLAB Symposium on the Exploration of Halley's Comet*, ESA SP-250
- Gombosi, T.I. 1994, *Gaskinetic Theory*, Cambridge University Press, Cambridge, UK
- Ip, W.-H. 2004, *Advances in Space Research*, 33, 605
- Jia, Y.D. 2007, *J. Geophys. Res.*, 112, A05223
- Johnstone, A. et al. 1986, *Nature*, 321, 344
- Klimov, S. et al. 1986, *Nature*, 321, 292
- Lesieur, M. 1990, *Turbulence in fluids*, 2nd ed., Kluwer, Dordrecht, The Netherlands
- Meyer-Vernet, N. 1986, *Science*, 232, 370
- Perez-de-Tejada, H. 1989, *J. Geophys. Res.*, 94, A10131
- Perez-de-Tejada, H. 1995, *Space Sci. Rev.*, 72,655
- Perez-de-Tejada, H. 1999, *ApJ*, 525, L65
- Perez-de-Tejada, H. 2000, *Planet. Space Sci.*, 48, 871
- Perez-de-Tejada, H. 2005, *ApJ*, 618, L145
- Perez-de-Tejada, Orozco, A., Dryer, M. 1980, *Astrophys. Space Sci.*, 68, 233
- Perez-de-Tejada, H. et al. 2009, *J. Geophys. Res.*, 114, A02106
- Reme, H. 1991, in *Cometary Plasma Processes*, ed. A.D. Johnstone, p. 86, AGU monograph 61, AGU, Washington, D.C.
- Reyes-Ruiz, M. et al. 2008, *Astron. Astrophys.*, 489, 1319
- Scarf, F.L. et al. 1986, *Science*, 232, 377
- Chunk, R.W. 1977, *Reviews of Geophysics and Space Physics*, 15, 429
- Chunk, R.W., Nagy, A.F. 1980, *Reviews of Geophysics*, 18, 813
- Shapiro, V.D. et al. 1995, *J. Geophys. Res.*, 100, 21289
- Slavin, J.A. et al. 1986, *Geophys. Res. Lett.*, 13, 283
- Spitzer, L. 1962, *Physics of Fully Ionized Gases*, 2nd edition, Interscience Publishers, New York
- Spreiter, J. & Stahara, S. 1980, *J. Geophys. Res.*, 85, 7715
- Szego, K. et al. 2000, *Space Sci. Rev.*, 94,429
- Tsurutani, B.T., Smith, E.J. 1986, *Geophys. Res. Lett.*, 13, 263
- Van Loo S. 2009, *MNRAS*, 395, 319
- Wallis, M.K. 1973, *Planet. Space. Sci.*, 21, 1647
- Wegmann, R. 2002, *Astron. Astrophys.*, 389, 1039

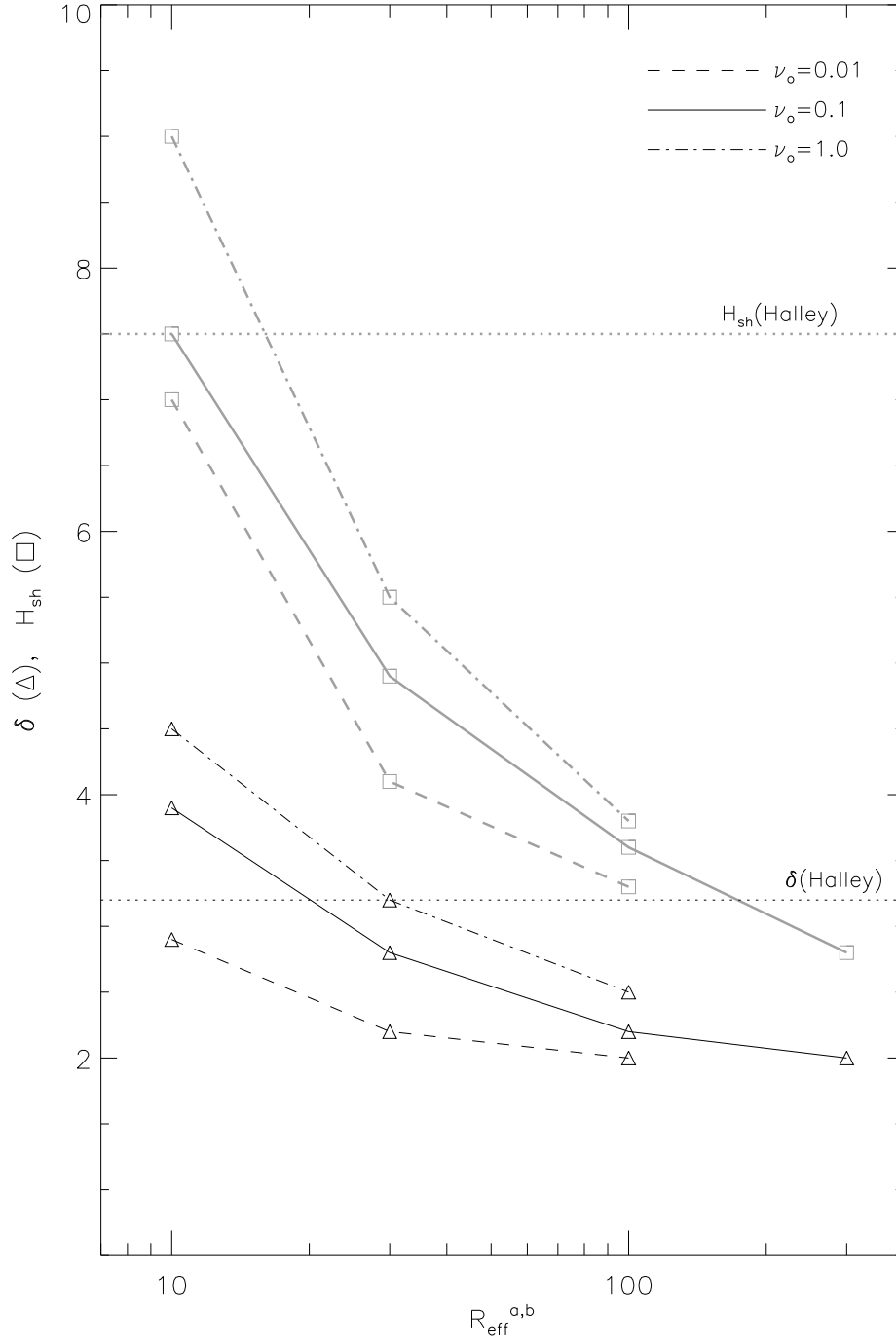


Fig. 11. Height of the shock front, H_{sh} (gray lines with squares) and thickness of the boundary layer, δ (black lines with triangles), as a function of effective Reynolds number, for a set of models with different value for the inter-species coupling parameter, ν_o . Values for these scale-heights correspond to $x = 5$ in our model. The dotted lines indicate the height of the shock front (gray) and the location of the intermediate transition (black) during the inbound portion of Giotto's flyby through the tail of comet Halley.